

Automatic Algorithm for Correcting Motion Artifacts In Time-Resolved 2D MR Angiography Using Convex Projections

Ashish Raj^{1,2}, Honglei Zhang¹, Martin R Prince¹, Yi Wang^{1,3}, Ramin Zabih^{1,4}

¹Radiology, Weill Medical College of Cornell University, New York, NY

²Electrical Engineering, Cornell University, Ithaca, NY

³Biomedical Engineering, Cornell University, Ithaca, NY

⁴Computer Science, Cornell University, Ithaca, NY

* Corresponding author:

Yi Wang

575 Lexington Avenue, 3rd floor

New York, New York 10022

Email: yiwang@med.cornell.edu

Phone: (646) 253 2809

Word Count: 6050

To appear in *Magnetic Resonance in Medicine*

POCS Motion Correction in 2D MRA

Automatic Algorithm for Correcting Motion Artifacts In Time-Resolved 2D MR Angiography Using Convex Projections

Abstract

Time-resolved contrast enhanced Magnetic Resonance Angiography (MRA) may suffer from involuntary patient motion. It is noted that while MR signal change associated with motion is large in magnitude and has smooth phase variation in k-phase, signal change associated with vascular enhancement is small in magnitude and has rapid phase variation in k-space. Based upon this observation, a novel POCS (projection onto convex sets) algorithm is developed as an automatic iterative method to remove motion artifacts. The presented POCS algorithm consists of high pass phase filtering and convex projections in both k-space and image space. Without input of detailed motion knowledge, motion effects are filtered out, while vasculature information is preserved. The proposed method can be effective for a large class of non-rigid motions, including through-plane motion. The algorithm is stable and converges quickly, usually within five iterations. A double-blind evaluation on a set of clinical MRA cases shows that a completely unsupervised version of the algorithm produces significantly better rank scores ($p = 0.038$) when compared to angiograms produced manually by an experienced radiologist.

Keywords: Convex Projections, POCS, motion correction, Magnetic Resonance Angiography.

INTRODUCTION

Time-resolved contrast enhanced Magnetic Resonance Angiography (MRA) provides temporal flow and anatomic information about vascular conduits (1). In projection 2D MR Digital Subtraction Angiography (MRDSA) (2,3), complex subtraction of pre-contrast from post-contrast data yields the arteriogram. Clinical evidence (4) indicates 2D MRDSA is as suitable for infrapopliteal imaging as conventional X-ray angiography. Patient motion can cause spurious changes in contrast-induced dynamic signal, contaminating the integrity of dynamic data relating to vascular evolution. Motion of elongated structures (e.g. bones) can create subtraction artifacts resembling arteries. The radiologist may be forced to discard motion-corrupted frames, causing gaps in the temporal MRA record and possibly misdiagnosis (5). Techniques that can rescue these motion-corrupted frames would be very valuable.

A range of motion correction methods have been developed, most of them utilize specific motion modeling. Correction of rigid global motion in single-frame MR images was reported using subspace analysis (6,7) and navigator-based correction (8,9,10). Motion in MRA may be non-global (affecting some but not all portions of image space) as well as inter-view motion (i.e. affecting some lines of k-space but not others). Global, rigid inter-view motion was addressed in a model-free manner using projection or entropy minimization (11,12,13,14,15), but these work did not address non-rigid motion typically encountered in MRA. Multi-sensor techniques for PET images (16) and cardiac gating using EEG (17, 18) may be applied to MRA, but require additional instrumentation with questionable effectiveness. Retrospective techniques (18) relying on correlation-based template matching of moving regions are inapplicable for inter-view motion, since motion occurs not only *between* frames but also *within* them. No existing works, to our knowledge, have addressed the case of inter-view motion that is non-global in image space. Currently for 2D MRDSA, frames corrupted by motion are identified and discarded manually (5).

We present here an automated iterative POCS (projection onto a convex set) algorithm that filters out motion artifacts in time series 2D MRDSA. The class of POCS algorithms has been used widely for band-limited extrapolation (19), image restoration (20), non-coherent phase correction in optics, and Partial Fourier MR techniques (21,22). The success of POCS in diverse applications

stems from its conceptually simple but powerful way to exploit *a-priori* constraints. Rather than attempt to track highly complex 3D motion parameters from 2D data, we exploit the dynamic information content of the MRDSA data set to retrospectively mitigate motion, however it may arise. This non-parametric approach treats motion simply as sources of k-space discrepancy, hence it is robust against in- and through-plane inter-view motion, both global and non-global. We take special care to ensure that vascular enhancement is not unduly affected in the process. We also prove convergence and stability of the algorithm.

THEORY

The proposed method relies on the following observations summarized from our extensive experience with time resolved contrast enhanced MRDSA:

1. Within the temporal MRA frames a majority of frames are “good”, i.e. motion-free.
2. Motion-free frames are nearly identical to each other except in vascular regions.
3. Contrast-induced vascular enhancement yields small changes in MR signal, with the change widespread in k-space. But motion usually causes much larger variations in detected signal.
4. Phase changes due to translational motion are either linear or smoothly-varying in k-space, whereas those due to vascular enhancement are sharply rapidly varying in k-space.
5. Out-of-plane components of 3D translations do not degrade 2D projection MRA data.

We now develop projections P_1 to P_4 that exploit observations 2-5 to remove motion artifacts from the corrupted frame by enforcing similarity to the “good” frames (observation 1) without degrading the vasculature. Each projection forces the corrupted frame to belong to a certain convex constraint set, convexity being required in POCS theory for guaranteed convergence (23,24). See Appendix A for definition and proof. The POCS algorithm is applied to the corrupted frame using a reference obtained from the “good” frames. For every corrupted frame c in the MRA sequence, let the starting image be $I_0 = I^c(x,y)$. At n -th iteration, the projections are

$$\left. \begin{aligned}
F_n^{(0)} &= FFT\{I_{n-1}\} \\
F_n^{(1)} &= (1 - \lambda_1) F_n^{(0)} + \lambda_1 P_1 F_n^{(0)} \\
F_n^{(2)} &= (1 - \lambda_2) F_n^{(1)} + \lambda_2 P_2 F_n^{(1)} \\
I_n^{(0)} &= IFFT\{F_n^{(2)}\} \\
I_n^{(1)} &= (1 - \lambda_3) I_n^{(0)} + \lambda_3 P_3 I_n^{(0)} \\
I_n^{(2)} &= (1 - \lambda_4) I_n^{(1)} + \lambda_4 P_4 I_n^{(1)} \\
I_n &= I_n^{(2)}
\end{aligned} \right\} \quad [1]$$

where $0 < \lambda_i < 1$, $i = 1, \dots, 4$, are relaxation factors used to weight the projections. This process is repeated many times. P_1 and P_2 are applied view-by-view in k-space, whereas P_3 and P_4 are applied on the full image. These highly independent constraint sets defined by P_1 -- P_4 , applied alternately in two orthogonal spaces (k-space and image space) form a powerful combination against motion artifacts. Figure 1 summarizes the algorithm.

P_1 : K-space Box Constraint Step

Observation 3 is used to design P_1 , which filters out large motion artifacts in k-space without using a specific parametric motion model. Letting $F(k_x, k_y)$ be the k-space image, we apply the projection

$$P_1(F) = \begin{cases} F & |F - F_{ref}| \leq \varepsilon |F_{ref}|; \\ F_{ref} + (F - F_{ref}) \frac{\varepsilon}{|F - F_{ref}|}, & |F - F_{ref}| > \varepsilon |F_{ref}|. \end{cases} \quad [2]$$

where F_{ref} is reference k-space data. Projection P_1 (**k-restrict**) is a non-linear k-space filter that restricts corrupted k-values to lie within a spherical ‘‘box’’ of reference k-values (see Figure 2). The box radius around f_{ref} is $\varepsilon |f_{ref}|$, $0 < \varepsilon < 1$. Box constraints of this kind are well known to be convex (13). Note that the efficacy of P_1 is unaltered by whether motion is in-plane or through-plane.

Since P_1 keeps large temporal changes from occurring, its application in general will lead to loss and obliteration of temporal events along with motion artifacts. However, observation 3 indicates that the vasculature is sparse and localized in image space, so its contribution to each k-space point is likely to be very small and widely spread. We empirically verify this observation in the next section and demonstrate that for a sensible choice of ε sufficiently larger than the mean energy per data point of the vasculature, P_1 will not adversely affect temporal evolution of the vasculature.

P₂ : Phase Correction Step

Projection P_2 , denoted by the box **phase-correct**, is a phase filter for correcting in-plane translational motion artifacts. It relies on observation 4, that phase artifacts due to translation vary smoothly in k-space (i.e. are band-limited to low spectral components), whereas the phase due to vascular evolution on subtracted images has much sharper k-space variation. We show this in the Results section by plotting the spectral distribution of phase difference (Figure 6). Clearly high-pass filtering this phase difference effectively suppresses translation phase. We selected a high-pass filter having a 5-point impulse response kernel in k-space given by $h = [-0.2, -0.6, 1, -0.6, -0.2]$, and the spectral response shown in Figure 3. This filter acts on the phase difference between the current and reference echo. Let the current frame be $F(k_x, k_y) = |F(k_x, k_y)| \cdot \exp\{i\phi(k_x, k_y)\}$.

Dropping coordinates, P_2 is given by

$$\begin{aligned} \Delta\phi &= \phi - \phi_{ref}, \\ P_2 F &= |F| \cdot \exp\{i(\phi_{ref} + h * \Delta\phi)\} \end{aligned} \quad [3]$$

where $*$ denotes convolution. h may be a 1D filter that acts only in the phase encode k_y direction. It is usually assumed that a single k_y line is acquired quick enough that motion effects occur *between* k_y lines, not *within* them (13). Filtering only along k_y prevents corrupted PE lines from influencing the phase of other k_y lines. In general, P_2 can be applied on both phase encoding and frequency encoding directions to filter out constant, linear and other smoothly varying phase in k-space. This P_2 filter can be effective against *non-global* translation (observation 4) (see empirical verification in Fig.6 and theoretical analysis in appendix B). Detailed spectral analysis was earlier reported in (25).

Convexity is vital for convergence and stability; unfortunately proving it is difficult due to non-linearity of P_2 . In Appendix A we provide a proof based on approximations. Now 2D projection MRA is the orthographic projection of 3D data after spatial averaging along the normal. Thus any translation normal to this plane does not affect the scan, provided the A-P projection slab is thicker than the range of through-plane translations, thus confirming observation 5.

P₃ and P₄: Intensity Correction Steps

Projection P_3 , **parenchyma-correct**, imposes image intensity constraints given by observation 2 by forcing the parenchyma (flesh) regions of the image to be “close” to the corresponding regions of

the reference. Let \wp be the set of all pixels belonging to regions deduced to be parenchyma. Then for every pixel p in the corrupted image and the corresponding pixel p_{ref} in the reference image

$$P_3(p) = \begin{cases} I(p), & p \notin \wp; \\ I(p), & p \in \wp, \quad |I(p) - I(p_{ref})| \leq \eta |I(p_{ref})|; \\ I(p_{ref}) + \eta \frac{I(p) - I(p_{ref})}{|I(p) - I(p_{ref})|}, & p \in \wp, \quad |I(p) - I(p_{ref})| > \eta |I(p_{ref})|. \end{cases} \quad [4]$$

This constraint set is well-known to be convex. For sequences without excessive motion a reference angiogram is usually available to drive reasonable estimates of parenchyma regions. The background is the MR region with no signal, and is non-zero merely due to noise and motion. Projection P_4 , **BkGnd** in Figure 1, forces it to be zero. This clearly defines a convex set, since a linear combination of two images of zero background is also an image of zero background.

MATERIALS AND METHOD

To validate the POCS method we performed several imaging experiments using a time resolved 2D MRDSA sequence. Both simulation and clinical MRA data were used. These experiments are categorized in 3 groups: 2D MRA signal characterization experiments, motion simulations, and in vivo clinical studies.

Signal Characterization of Peripheral 2D MRA Data

In order to validate the observations presented in Theory section, clinical peripheral 2D MRA data of the tibial trifurcation was studied. We examined the magnitude and phase of signals arising from the vasculature as well as from motion-induced artifacts. An uncorrupted exam was used to validate observation 3. The angiogram was obtained manually, and this served as a model for vasculature signal. K-space magnitude of this, as well as overall magnitude data, was plotted on the same axis, by averaging 4 radial k-space lines. A motion corrupted angiogram displaying non-global translation in image space was similarly processed for comparison. To validate observation 4, spectra of phase difference due to vascular enhancement between adjacent frames was obtained using Burg's average periodogram (26) from several rows of vasculature phase in k-space.

Spectrum of translation-induced phase was obtained; details are in Appendix B. Relevant plots are presented in the results section.

Validation on simulated motion

Motion free clinical MRA data was used to artificially introduce various kinds of motion. POCS was applied to these data sets. We varied λ from 0 to 1 in 0.1 increments, ε from 0 to 0.5 in 0.05 increments and η from 0.5 to 1 in 0.05 increments for a number of cases, and selected the parameters yielding the best overall results by visual inspection. These parameters are: $\lambda_1 = \lambda_2 = \lambda_3 = \lambda_4 = 0.8$, $\varepsilon = 0.25$, $\eta = 0.75$. Unless otherwise noted, all results herein and henceforth used these parameters, with 3 iterations of POCS.

We studied three kinds of motion: step translation, random walk translation, and combined translation and rotation; all with non-global inter-view motion. In order to introduce non-global motion, the original raw data is Fourier transformed into image-space. The first simulation introduces a translation in the top half of the image by 2 pixels in both x- and y-directions, then the image is transformed back to k-space. To simulate step-type inter-view motion, we replaced the top 40% of the views by those of the original data. Next we apply a continuous random-walk translation in the same manner, which is plotted against PE index in Figure 4(a). The step size at each point was sampled from a zero mean Gaussian to model erratic or involuntary motion. Finally 15° rotation of the top half of the image corresponding to the left leg was introduced before the translation simulated in the first experiment. The k-space data now consists of the top part unaffected by motion, the middle part affected by translation and rotation, and the bottom part affected by translation only. The resulting effect on k-space data is depicted in 4(b).

Validation on Clinical MRDSA Data

Real clinical peripheral MRA exams of the trifurcation were done on 47 consecutive patients (26 males aged 24 - 87 years and 19 females aged 33 - 85 years). Primary indications in these patients included claudication (n=23), limb threatening ischaemia (n=11), aneurysm (n=7), post-bypass graft (n=3), and dissection (n=1). The study was approved by our Institutional Review Board. The 2D projection MRA data were obtained at 1.5 Tesla using a head coil (LX Horizon, GE Medical Systems). Patients were placed feet-first with legs positioned within the head coil to image from

above the patella down to mid-calf. The 2D projection MRA was performed as a coronal spoiled gradient echo sequence using the following parameters: TR/TE/ flip angle = 10/2/60 degrees, slab thickness = 7-10 cm, field-of-view = 30cm, matrix = 256x192, bandwidth = 16 kHz. Imaging time was 1.95 seconds per acquisition repeated 35 times. Gadolinium contrast (5-7 ml at 0.5mol/L) (Magnevist, Berlex Labs, Wayne, NJ) was injected concurrent with image acquisition and flushed with 20 ml saline. The injection rate was 2.5ml/sec by hand with a SmartSet (TopSpins, Ann Arbor, MI) or using an automatic injector (Spectris MR Injector, MedRad, Pittsburgh, PA). Five to ten pre-contrast frames were obtained.

MRA data was processed in two ways: manual (5) and automatic. First, MRA frame sequences were visually evaluated by an experienced radiologist (HZ), and estimates of contrast arrival, arterial, mask and venous phase were manually obtained. After discarding motion-corrupted frames, the final angiogram was obtained by subtracting mask frames from arterial frames. Next, for automatic motion correction, mask and arterial phases were identified using (27), a new, automatic MRDSA method. We incorporated the proposed POCS algorithm within this automated MRDSA algorithm. Our implementation ran 3 iterations of POCS on all frames identified by the automatic MRDSA software as having motion, with $\lambda = 0.8$, $\varepsilon = 0.25$, $\eta = 0.75$. The reference was obtained, after some experimentation, by median operation on the preceding 3 frames.

To assess the difference between manual motion and automatic correction, a double blinded study was performed on 47 cases. Randomized image pairs from both manual and automatic corrections were presented to another experienced radiologist (MRP). The images were ranked from 2 to -2, with 2 denoting one method performing substantially better than the other, 1 (marginally better), 0 (same), -1 (marginally worse) and -2 (substantially worse). A one-sided paired signed-rank Wilcoxon test was performed on this data to assess the statistical difference between manual and automatic motion correction.

RESULTS

Signal Characterization of Peripheral 2D MRA Data

Figures 5(a-b) show an uncorrupted and a corrupted angiogram respectively. The k-space magnitude of both reference and difference (vascular) signal of (a) is plotted in (c). Observe that apart from one or two central pixels containing the lowest frequencies, the vascular curve maintains nearly constant low energy. In contrast, the reference data follows a more pronounced decline in magnitude. In (d) we plot the ratio of uncorrupted vasculature to reference magnitude, averaged over several radial lines of several angiograms. The highest point of the curve is lower than 0.25; hence $\varepsilon > 0.25$ will ensure against vascular degradation. Part (e) shows the ratio curve of the corrupted case (b). The corrupted ratio is much higher, an average of 20 times, than pure vascular ratio. This was generally observed in the other cases we investigated, thus confirming observation 3. Figure 6(a) shows a spectrum of phase (after unwrapping) caused by non-global in-plane translation, and (b) shows the spectrum of the phase caused by the vasculature.

Results of Simulated Motion

The POCS algorithm is quite effective in removing artifacts from the three types of simulated motion, as shown in Figure 7. Step translation on uncorrupted frame (a) results in a corrupted angiogram (c) after frame subtraction, which is diagnostically useless compared to the uncorrupted angiogram (b). Even though only the top half of the image undergoes translation, due to inter-view motion the effect is uniformly bad for the entire image. Part (d) shows the POCS-corrected result. Angiogram corrupted by random-walk translation is in (e) and POCS corrected angiogram in (f). Images for the combined rotation/translation example are in (g) and (h). Due to partial k-space effect, the artifacts in (g) are more disturbing than mere rotational mis-alignment, the latter being visible in the top half, aligned at roughly 15° . POCS removes most artifacts in all three cases.

Results of Automatic versus manual Motion Correction on Clinical MRDSA Data

Result of the double-blinded comparison is summarized in Table 1. Improvement in visual quality as well as SNR was observed in most cases exhibiting motion artifacts. Two representative examples are illustrated in Figs.8&9. Figure 8 shows substantial motion artifacts, whereas Figure 9 shows little motion. The results on a typical consecutive difference image from this data set are shown in Figs.8a&8b. As a consequence of such improvements in individual frames, POCS yielded a markedly cleaner automatic summary angiogram (Fig.8d) than the manual angiogram (Fig.8c). The case of Figure 9 shows the left leg having an occluded posterior tibial artery. There are few artifacts to begin with; POCS yielded slightly better subjective quality (from the double-blinded

evaluation) on account of minor improvements in background noise. The one-sided paired signed-rank Wilcoxon test on this data indicates statistically significant improvement of POCS over manual ($p = 0.04$).

DISCUSSION

We have presented a POCS algorithm that can filter out motion artifacts from 2D time resolved contrast enhanced MRA. This POCS algorithm is based on the observations that large magnitude changes and smooth phase variations in detected k-space signal are associated with motion, while small magnitude changes and rapid phase variations in k-space signal are associated with contrast enhancement. Simulated motion experiments indicate the POCS algorithm provides clear removal of arbitrary artifacts from a variety of motion sources. Evaluation on clinical MRDSA data suggests that the automatic POCS provides significant artifact reduction.

Though overall the POCS algorithm significantly outperformed an experienced radiologist in the clinical evaluation, quality improvement in the summary angiogram was not observed in all cases (Table 1). In cases that the automatic POCS did slightly worse than manual, there were not much motion artifacts to begin with. Since it is necessary to constrain the time evolution of vascular features to remove arbitrary motion, there may be slight loss of fine details in vascular definition in the process of repeat applications of the POCS algorithm on the same data set. This is a problem only for incessant, pervasive motion, a relatively infrequent occurrence. In the clinical data set investigated in this study, our POCS algorithm caused little vascular degradation.

Phase unwrapping has to be performed prior to high-pass filtering. While unwrapping is a difficult problem in general (28, 29), a simple method was found sufficient by smoothing out simple π -jumps along the k_y direction in a center-edge order. Experimentation with more sophisticated unwrapping methods did not result in discernible performance gains, probably because the phase difference is along the k_y only. This is a 1D unwrapping problem that does not require complicated phase unwrapping algorithms.

The parameters in the presented POCS algorithm were chosen empirically from the following range of variations: $\lambda_i \in [0.5, 1.0]$ ($i=1,2,3,4$), $\varepsilon \in [0.2, 0.5]$, and $\eta \in [0.5, 1.0]$. For the studied clinical cases, the algorithm performance in terms of convergence and artifacts removal was fairly insensitive to the variation in λ_i and η . For cases with pervasive (rather than isolated) motion, the output image quality varied slightly with the box radius ε . We also noted that the POCS algorithm performance was also insensitive to the bandwidth of the high-pass filter h . Indeed, a major goal of our work is to keep things *non-parametric* as far as possible.

Since P_1 -- P_4 are linear point-wise filtering operations, the algorithm is quite fast, taking approximately 3 sec / frame in a MATLAB implementation on a PC with 2GHz Pentium III[®] processor. We expect an efficient C execution to reduce this by more than an order of magnitude.

We have shown mathematically in Appendix B that global as well as non-global translations can be handled by projection P_2 . This discussion can be extended to rotation, which can be removed by the combination of P_2 and P_1 . P_1 filters out large rotations both in-plane and through-plane; the residual in-plane rotations are small and can be approximated by:

$$\vec{x}' = \vec{x} + |\vec{x}| \delta\phi \vec{\phi}_x$$

where \vec{x} is a 2D vector representing spatial location, the rotational angle is $\delta\phi$, and the direction of rotation at \vec{x} is given by the unit vector $\vec{\phi}_x$. Since this is nothing but a piecewise non-global translation, it can subsequently be removed by P_2 .

The assumption that an uncorrupted reference image can be obtained from the median operation may fail if there is excessive motion in all or a majority of frames in the pre-contrast reference set. Such situations appear to be rare. The median operation on the reference set ignores isolated instances of motion in the reference set. The number of frames for reference is selected to average out the noise but avoid motion contamination. We found that 3 reference frames worked well in our clinical evaluation.

The fully automatic motion filtering presented here used input of contrast arrival frame number to classify pre-contrast frames for reference. The automated estimate of contrast arrival may be

unreliable in the presence of motion (27). The POCS algorithm can be applied in non-automatic mode, where an operator selects arterial, mask and motion-corrupted frames.

The retrospective POCS algorithm can be used synergistically with the navigator gating method such as to minimize residual motion artifacts within the gating window (30). This non-parametric POCS method may be more advantageous than existing parametric motion correction methods (10) in cases when object motion cannot be completely determined. The POCS algorithm may also be applied to reduce motion artifacts in other dynamic studies such as fMRI and perfusion.

Generalization to 3D data and complex 3D motion should be quite straightforward since we do not rely on specific motion models. These generalizations of the POCS approach will require modification of the projection operators.

In conclusion, vascular enhancement and motion artifacts affect k-space signal magnitude and phase in a distinct manner. Accordingly, a POCS algorithm can be constructed that imposes consistency constraints in dynamic MRA data to filter motion artifacts but preserve vascular enhancement. Clinical data demonstrated the feasibility of using the model-free POCS algorithm to suppress arbitrary motion artifacts.

Appendix A: Convex Constraint Sets – Definition and Proof

For a frame of $N \times M$ voxels, imagine an NM -variable solution space, each of whose points represents a possible image. In POCS theory projections are defined by constraints, which force possible solutions to belong to some convex *constraint set* in this solution space. A set C is convex iff for any two members $a, b \in C$ a binary mixture $c = \alpha a + (1-\alpha) b$, $0 < \alpha < 1$, also belongs to C . Proving convexity of P_2 is complicated since it is a phase operator and not guaranteed to define a convex projection in \square^{MN} , the space of $M \times N$ complex images. Theorem 1 proves that it does in fact approximate, to arbitrary accuracy, a convex projection by virtue of algorithm construction.

Theorem 1: Let $H(\phi(k_x, k_y))$ be the high pass filter (P_2) applied on phase $\phi(k_x, k_y)$. Let L be the complementary low-pass filter constructed such that $LH = 0$, and C the set of $M \times N$ complex k-space frames of identical magnitude $M(k_x, k_y)$, $k_x = 1 \dots M$, $k_y = 1 \dots N$ such that $C = \{M(k_x, k_y) \exp\{i\phi_0(k_x, k_y) + i\phi(k_x, k_y)\} \mid L(\phi(k_x, k_y)) = 0\}$. Dropping the indices (k_x, k_y) henceforth,

1. The phase correction step defines a projection onto C .
2. Set C approximates a convex set over a region of interest $R \subseteq C$ containing members with phase bounded by ϕ_{max} : $\phi_{max} \leq \phi \leq \phi_{max}$. The error of approximation is proportional to ϕ_{max}^2 .
3. The k-space box projection P_1 with box radius ε imposes a bound ϕ_{max}^2 on the phase of the intermediate POCS solution at every iteration, with $\phi_{max} = \varepsilon$.

Proof: 1. For any $A = M \exp(i(\phi_0 + \phi))$, we have $A' = M \exp(i(\phi_0 + H(\phi))) \in C$, since $L(H(\phi)) = 0$. Hence P_2 defines a projection onto C .

2. Let $A_1 = M \exp(i(\phi_0 + \phi_1))$, $A_2 = M \exp(i(\phi_0 + \phi_2))$ be two members of C . We need to show that $\bar{A} = \alpha A_1 + (1-\alpha)A_2$ also belongs to C . We have $\bar{A} = M \exp(i\phi_0) [\alpha \exp(i\phi_1) + (1-\alpha) \exp(i\phi_2)]$

Linearizing the expression within square brackets by the Taylor Series we obtain

$$(\alpha + 1 - \alpha) + (\alpha\phi_1 + (1-\alpha)\phi_2) - \frac{i}{2}(\alpha\phi_1^2 + (1-\alpha)\phi_2^2) + \text{higher order terms}. \quad [\text{A1}]$$

Higher order terms can be safely omitted for small ϕ_1 and ϕ_2 . Expanding this in a Taylor Series in $(\alpha\phi_1 + (1-\alpha)\phi_2)$ by completing the square for quadratic terms and omitting higher terms,

$$\bar{A}_1 = M \exp(i\phi_0) \{\exp(i(\alpha\phi_1 + (1-\alpha)\phi_2)) + E\}, \quad [\text{A2}]$$

where the error term E is the residue from completing the square. Clearly \bar{A}_1 belongs to C up to error E , since $L(\alpha\phi_1 + (1-\alpha)\phi_2) = 0$. It follows easily that $E = \frac{\alpha(1-\alpha)}{2}(\phi_1 - \phi_2)^2$. Given that

$-\phi_{max} \leq \phi_1, \phi_2 \leq \phi_{max}$, clearly the maximum error $E_{max} = \phi_{max}^2$ occurs at $\alpha = 1/2$, $\phi_1 = -\phi_2 = \phi_{max}$.

3. From Figure 2, every k-space point f of any solution must reside within the circle of radius $\varepsilon/|f_{ref}|$ in the complex plane, where f_{ref} is the reference. Then the maximum phase difference between any two points in that circle is ϕ_{max} as shown in the figure. Since a tangent subtends a right angle at the center, $\sin(\phi_{max}) = \varepsilon$. Proof follows from small angle approximation of sines.

Appendix B: Analysis of Translational Phase

A global translation of (Δ_x, Δ_y) in image $I(x,y)$ and its k-space dual $K(k_x, k_y) = \mathcal{F}(I(x,y))$, leads to linear phase in k-space given by $K'(k_x, k_y) = K(k_x, k_y) \exp\{i c (\Delta_x k_x + \Delta_y k_y)\}$, for some constant c . This phase, a ramp in k-space, is obviously band-limited. Proving band-limitedness of non-global translation rigorously is difficult; we prove it for an N-piece translation model (25):

$$K'(k_x, k_y) = \sum_{i=0}^N K_i(k_x, k_y) \exp(ic\Delta_{x_i} k_x + \Delta_{y_i} k_y), \quad [\text{B1}]$$

where each K_i is the transform of an image piece undergoing translation by $(\Delta_{xi}, \Delta_{yi})$. As $N \rightarrow \infty$, [B1] obviously models *any* in-plane motion; however, allowing for piecewise rotations as well, even small N can accurately model complex motions like limb articulation, shifting, trembling, etc.

Definition: Let $\mathcal{Q}(W)$ be the set of 2D functions $\phi(k_x, k_y) : \mathbb{R}^2 \rightarrow \mathbb{R}$ whose Fourier Transform $\mathcal{F}(\phi)$ is limited to the low spectral band $[-W, W] \times [-W, W]$, with W being the cutoff frequency.

Proposition 2: The phase difference between the corrupted and reference frame, $\Delta\phi(K', K) = \phi(K') - \phi(K)$ belongs to $\mathcal{Q}(W)$, i.e., is band-limited. Consequently, the power spectral density of $\Delta\phi(K', K)$ is concentrated in the low spectral region $[-W, W] \times [-W, W]$.

To keep the analysis uncluttered, we only consider the two-piece model

$$K'(k_x, k_y) = K_1(k_x, k_y) \exp(i\phi_1(k_x, k_y)) + K_2(k_x, k_y) \exp(i\phi_2(k_x, k_y)) \cdot \exp(ic\Delta_x k_x + \Delta_y k_y), \quad [\text{B2}]$$

where $\phi(\cdot)$ denotes the phase, K_1 is the stationary component, and K_2 undergoes translation.

However, this does not cause loss of generality due to the following theorem (proved in (25)).

Theorem 2: If Prop. 2 holds for the 2-piece model [B2], it also holds for N-piece model [B1].

That is, the phase difference $\Delta\phi(K', K)$ is band-limited for [B1] as well: $\Delta\phi(K', K) \in \mathcal{Q}(W)$.

We now derive the phase $\Delta\phi = \phi' - \phi$ caused by the two-piece translation model [B2].

Expression For Phase Difference

We model $\phi(k_x, k_y)$ as a random process uniformly distributed in $[-\pi, \pi]$ with a power spectral density exhibiting 3 dB cutoff at angular frequency W_0 ; this is a popular stochastic model of phase. Let $\delta(k_x, k_y) = c(\Delta_x k_x + \Delta_y k_y)$ be the phase term due to translation. Let $\phi(k_x, k_y)$ and $\phi'(k_x, k_y)$ be the phase before and after motion. Theorem 3, proved in (25), summarizes the main result.

Theorem 3: Let δ, ϕ, ϕ' be defined as above, and let the phases of components K_1 and K_2 prior to translation be ϕ_1 and ϕ_2 respectively. Let $\alpha = |K_2| / |K|$ be the ratio of the moving signal strength to the overall signal strength. Then the overall phase change is

$$\Delta\phi = \sin^{-1} \left(\frac{\alpha(\sin(\phi - \phi_2) + \sin(\phi_2 - \phi + \delta))}{\sqrt{1 + 4\alpha^2 \sin^2(\delta/2) + 4\alpha \sin(\phi - \phi_2 - \delta/2) \sin(\delta/2)}} \right) \quad [\text{B3}]$$

General spectral analysis of [B3] is difficult, but demonstrative results were obtained for special cases corresponding to $|K_1| \gg |K_2|$, $|K_1| = |K_2|$ and $|K_1| \ll |K_2|$, covering all scenarios. We derived bandwidth formulas for each case and proved low leakage outside spectral band $[-W_0, W_0]$.

REFERENCES

1. Prince MR, Grist TM, Debatin JF. 3D Contrast MR Angiography. Springer-Verlag; 1998.
2. Wang Y, Johnston DL, Breen JF, Huston J, 3rd, Jack CR, Julsrud PR, Kiely MJ, King BF, Riederer SL, and Ehman RL. Dynamic MR digital subtraction angiography using contrast enhancement, fast data acquisition, and complex subtraction. *Magn Res Med* 1996; 36:551-556.
3. Hennig J, Scheffler K, Laubenberger J, and Strecker R. Time-resolved projection angiography after bolus injection of contrast agent. *Magn Res Med* 1997; 37: 341-145.
4. Zhang HL, Khilnani NM, Prince MR, Winchester PA, Golia P, Veit P, Watts R, Wang Y. Diagnostic accuracy of time-resolved 2D projection MR angiography for symptomatic infrapopliteal arterial occlusive disease. *AJR Am J Roentgenol.* 2005 Mar;184(3):938-47.
5. Yoo SK, Watts R, Winchester PA, Zabih R, Wang Y, Prince MR. Postprocessing techniques for time-resolved contrast-enhanced MR angiography. *Radiology* 2002; 222:564-568.
6. Zoroofi R. Cancellation of MRI artifacts in image plane. *IEEE Trans Med Imag* 1996;5:178-82.
7. Park N, Kim E. Cancellation of MRI motion artifact in image plane. *IEEE I&M Technical Conference Proceedings* 2002; 329–334.
8. Miller KL, Pauly JM. Nonlinear Phase Correction For Navigated Diffusion Imaging. *Magn Res Med* 2003; 50:343–353.
9. Hoge WS. A Subspace Identification Extension To The Phase Correlation Method. *IEEE Trans Med Imaging* 2003; 22(2):223–227.
10. Ehman RL, Felmlee JP. Adaptive technique for high-definition MR imaging of moving structures. *Radiology* 1989; 173:255-263.
11. Hedley M, Yan H, Rosenfeld D. Motion Artifact Correction In MRI Using Generalized Projections. *IEEE Trans Med Imaging* 1991; 10:40–46.
12. Weerasinghe C, Yan H. An Improved Algorithm For Rotational Motion Artifact Suppression In MRI. *IEEE Trans Med Imaging* 1998;17(2):310–317.
13. Weerasinghe C, Yan H, Ji L. Fast Method For Estimation Of Object Rotation Function In MRI Using A Similarity Criterion Among K-Space Overlap Data. *Signal Proc* 1999; 78:215–230.
14. Atkinson D, Hill DL, Stoye PN, Summers PE, Keevil SF. Automatic correction of motion artifacts in magnetic resonance images using an entropy focus criterion. *IEEE Trans Med Imaging.* 1997;16(6):903-10.

15. Manduca A, McGee KP, Welch EB, Felmlee JP, Grimm RC, Ehman RL. Autocorrection in MR imaging: adaptive motion correction without navigator echoes. *Radiology*. 2000;215(3):904-9.
16. Picard Y, Thompson CJ. Motion Correction Of PET Images Using Multiple Acquisition Frames. *IEEE Trans Med Imaging* 1997; 16(2):137-144.
17. Gmelin E, Weiss HD, Buchmann F. Cardiac Gating In Intravenous DSA. *Eur J Radiol* 1986;6(1): 24-29.
18. Meijering EH, Niessen WJ, Viergever MA. Retrospective Motion Correction In Digital Subtraction Angiography: A Review. *IEEE Trans Med Imaging* 1999; 18(1):2-21.
19. Ferreira PJ. Interpolation And The Discrete Gerchberg-Papoulis Algorithm. *IEEE Transactions in Signal Processing* 1994; 42(10):22-29.
20. Ratakonda K, Ahuja N. POCS-Based Adaptive Image Magnification. *Proc ICIP* 1998;1231-35.
21. Oskoui-Fard P, Stark H. Tomographic Image Reconstruction Using Convex Projections. *IEEE Trans Med Imaging* 1988; 7:45-58.
22. Xu Y, Haacke EM. Partial Fourier Imaging In Multi-Dimensions: A Means To Save A Full Factor Of Two In Time. *J Magn Res Med* 2001; 14:628-635.
23. Gubin LG, Polyak BT, Raik EV. The Method Of Projections For Finding The Common Point Of Convex Sets. *USSR Computational Mathematics and Mathematical Physics* 1967; 7:1-24.
24. Opial Z. Weak Convergence Of The Sequence Of Successive Approximations For Nonexpansive Mappings. *Bull American Mathematical Society* 1967; 73:591-597.
25. Raj A. A Signal Processing And Machine Vision Approach To Problems in Magnetic Resonance Imaging. PhD Thesis, Cornell University, May 2005.
26. Stoica P, Moses RL. *Introduction to Spectral Analysis*. New York: Prentice-Hall; 1997.
27. Kim J, Prince MR, Zabih R, Bezanson J, Watts R, Erel HE, Wang Y. Automatic selection of mask and arterial phase images for temporally-resolved MR digital subtraction angiography. *Magn Res Med* 2002; 48(6):1004-1010.
28. Hedley M, Rosenfeld D. A New Two-Dimensional Phase Unwrapping Algorithm For MRI Images. *Magn Res Med* 1992; 24(1):177-181.
29. An L, Xiang QS, Chavez S. A Fast Implementation Of The Minimum Spanning Tree Method For Phase Unwrapping. *IEEE Trans Med Imaging* 2000; 19(8):805-808.
30. Wang Y, Ehman RL. Retrospective adaptive motion correction for navigator-gated 3D coronary MR angiography. *J Magn Reson Imaging* 2000; 11:208-214.

Table Captions

Table 1: Double blinded comparison results. Scores: 2(POCS substantially better than manual), 1(marginally better), 0 (same), -1(marginally worse), -2(substantially worse).

| Rank Score | 2 | 1 | 0 | -1 | -2 | Mean |
|------------|---|----|---|----|----|-----------------|
| # cases | 3 | 22 | 6 | 16 | 0 | 0.26 (p=.04) |

Figure Captions

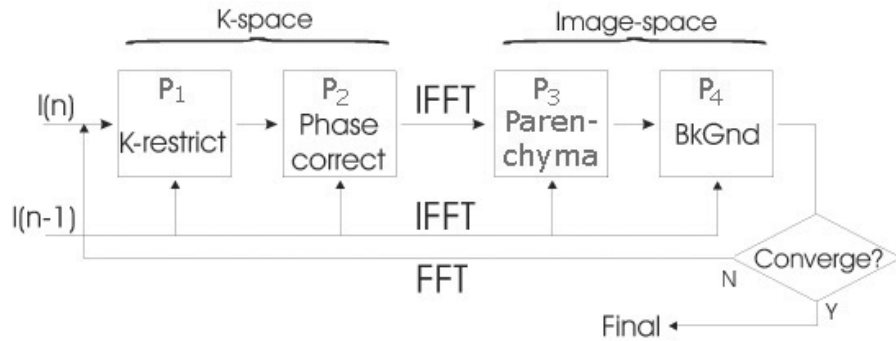


Figure 1: The POCS Algorithm. Each box represents a convex projection P_1 – P_4 . P_1 or “k-restrict” and P_2 or “phase-correct” operate in k-space, one view at a time. P_3 (parenchyma-correct) and P_4 (background-correct) operate in image space, on the entire image. FFT and IFFT operators perform Fourier Transform and its inverse, respectively. The POCS algorithm is repeated till a convergence criterion is met.

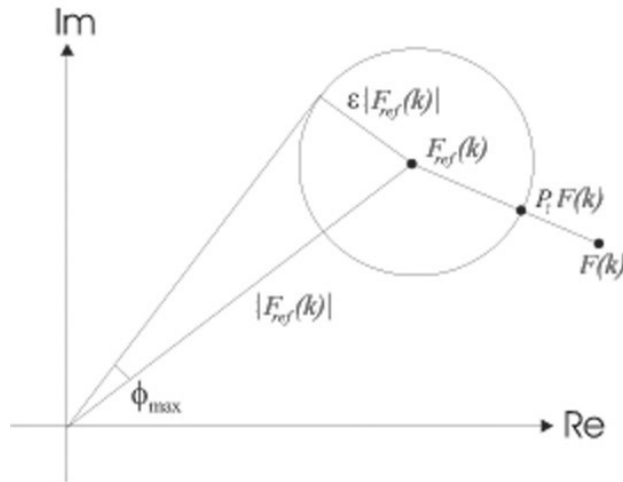


Figure 2: The k-space box constraint imposed by P_1 moves an arbitrary point $F(k)$ in the corrupted frame to the nearest point, denoted by $P_1 F(k)$, on the circle centered at the corresponding k-value in the reference image, $F_{ref}(k)$. This forces corrupted k-space to be similar to reference k-space. The parameter ϵ determines the degree of enforced similarity.

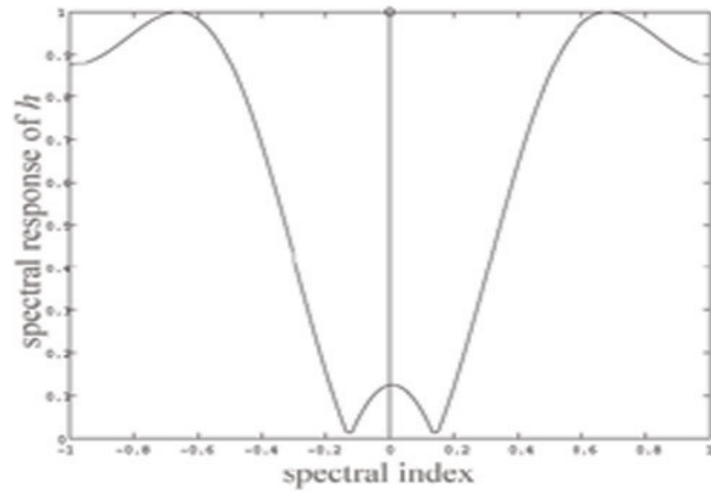


Figure 3: Spectral response of high-pass phase filter h . The spectral index has dimension of space.

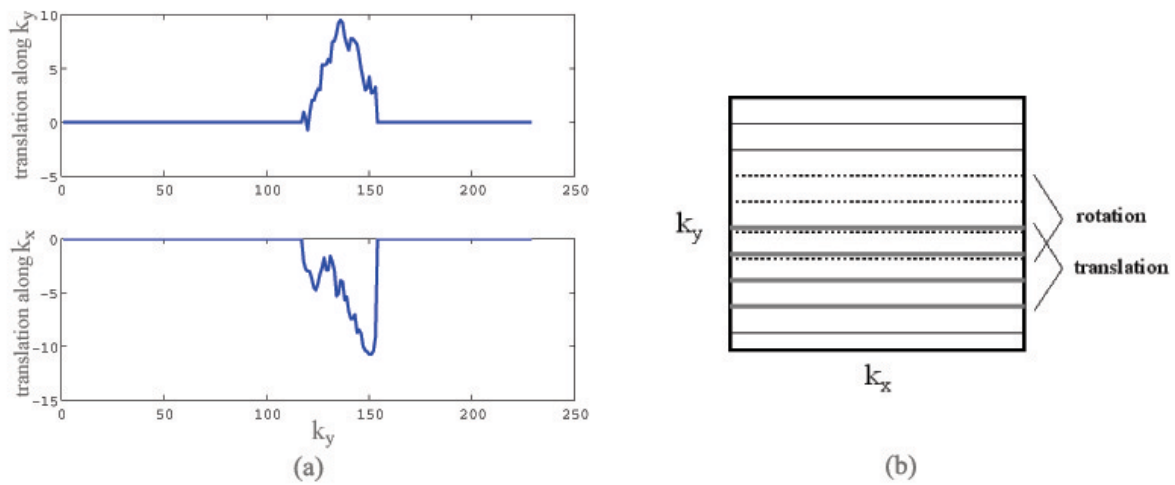


Figure 4:(a) Non-global random-walk translation, plotted as a function of k_y , the phase encode index (in units of $1/\text{FOV}$). It is assumed that motion is only *between* different PE lines, not *within* them. The top curve shows translation along PE; bottom curve along FE. (b) Combined non-global rotation and translation mapped in k-space.

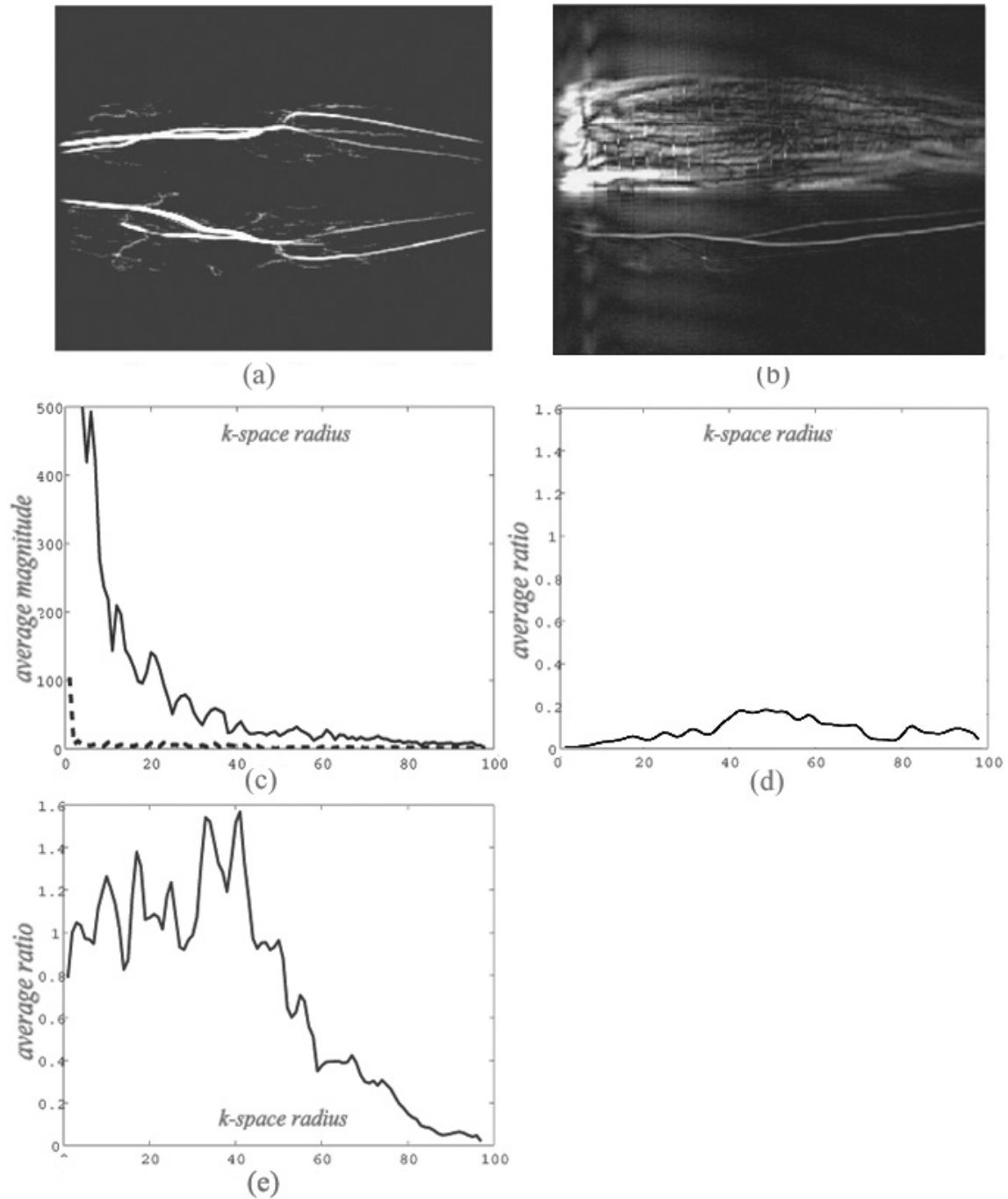


Figure 5: Signal properties of a typical peripheral 2D MRA case. (a) Uncorrupted difference image; (b) Difference image corrupted with non-global translation and rotation; (c) Plot of k-space magnitudes vs. radius for (a) (solid line: unsubtracted reference magnitude, dashed line: vascular signal); (d) ratio of vascular to reference magnitude for the uncorrupted case (a); (e) ratio of

vascular to reference magnitude for the corrupted case (b). The corrupted ratio is on average 20 times higher than the uncorrupted ratio.

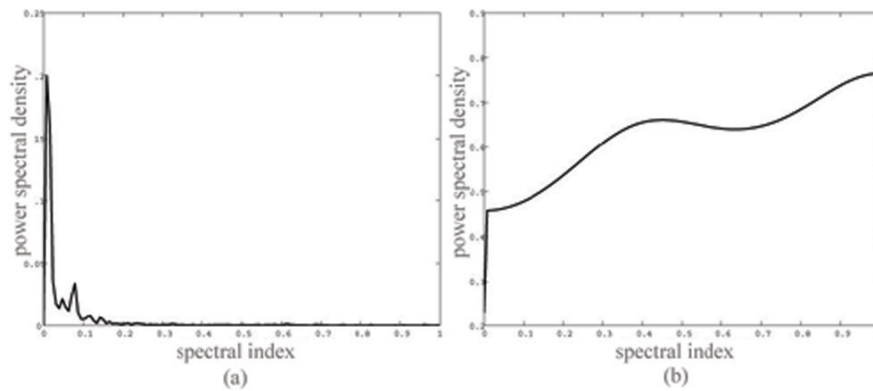


Figure 6: Typical power spectra of k-space signal phases, obtained from the phase difference between consecutive frames: (a) phase due to non-global translation in image space; (b) phase due to vascular enhancement, obtained from an artifact-free sequence. Spectra concentrated near low (high) spectral index correspond to slow (fast) phase variation across k-space. Note that although spectral index has spatial dimensions, a simple interpretation in terms of image-space properties is not available since the former indexes only phase data rather than the entire complex data.

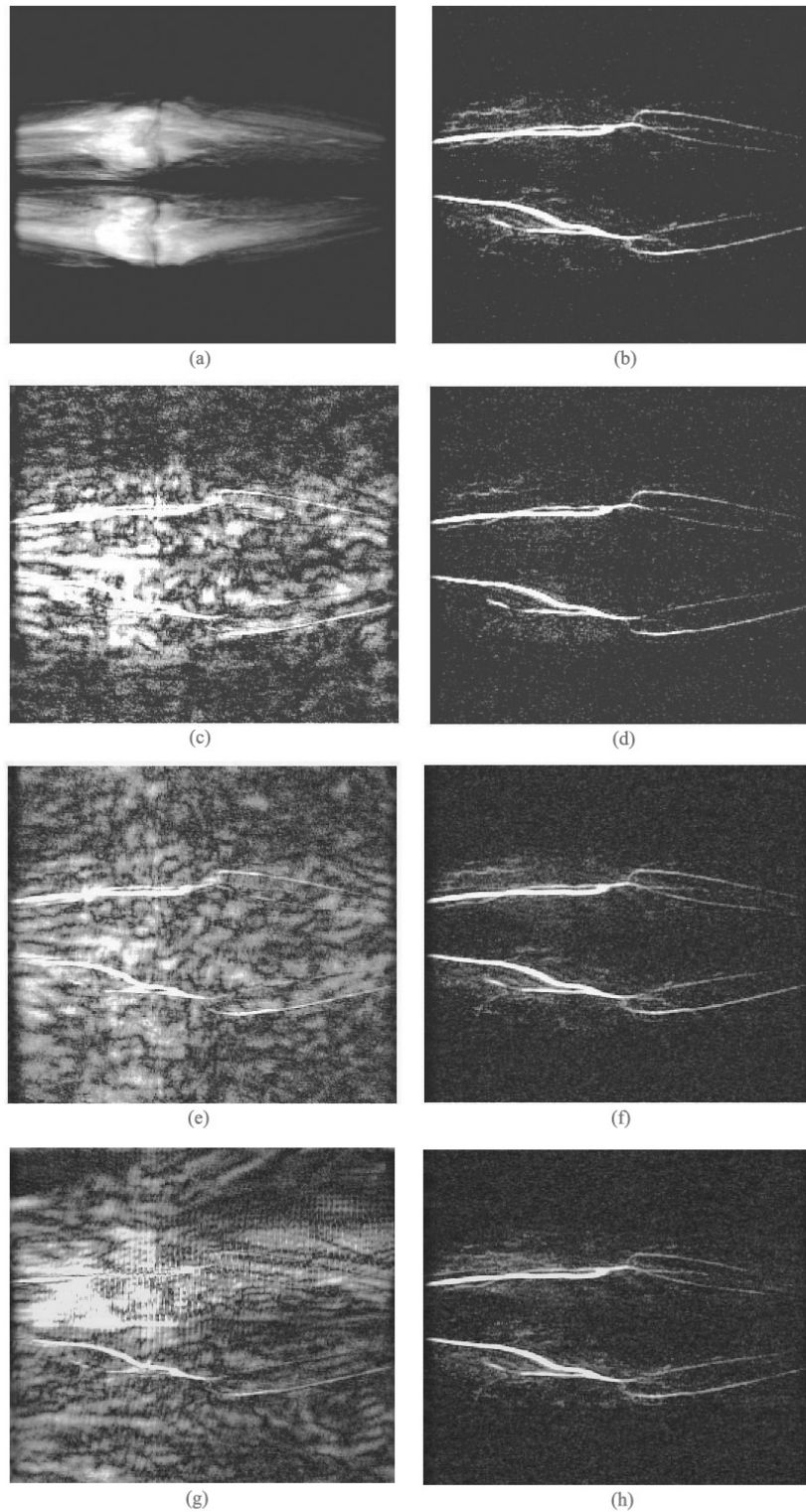


Figure 7: Examples of various types of non-global inter-view motion: (a) Uncorrupted frame, (b) Uncorrupted (single difference) angiogram, (c) Corrupted by step translation, (d) POCS result, (e) Corrupted by random-walk translation, (f) POCS result, (g) Combined translation + rotation, (h)

POCS result. POCS effectively removed most motion artifacts from these complicated examples of non-global motion.

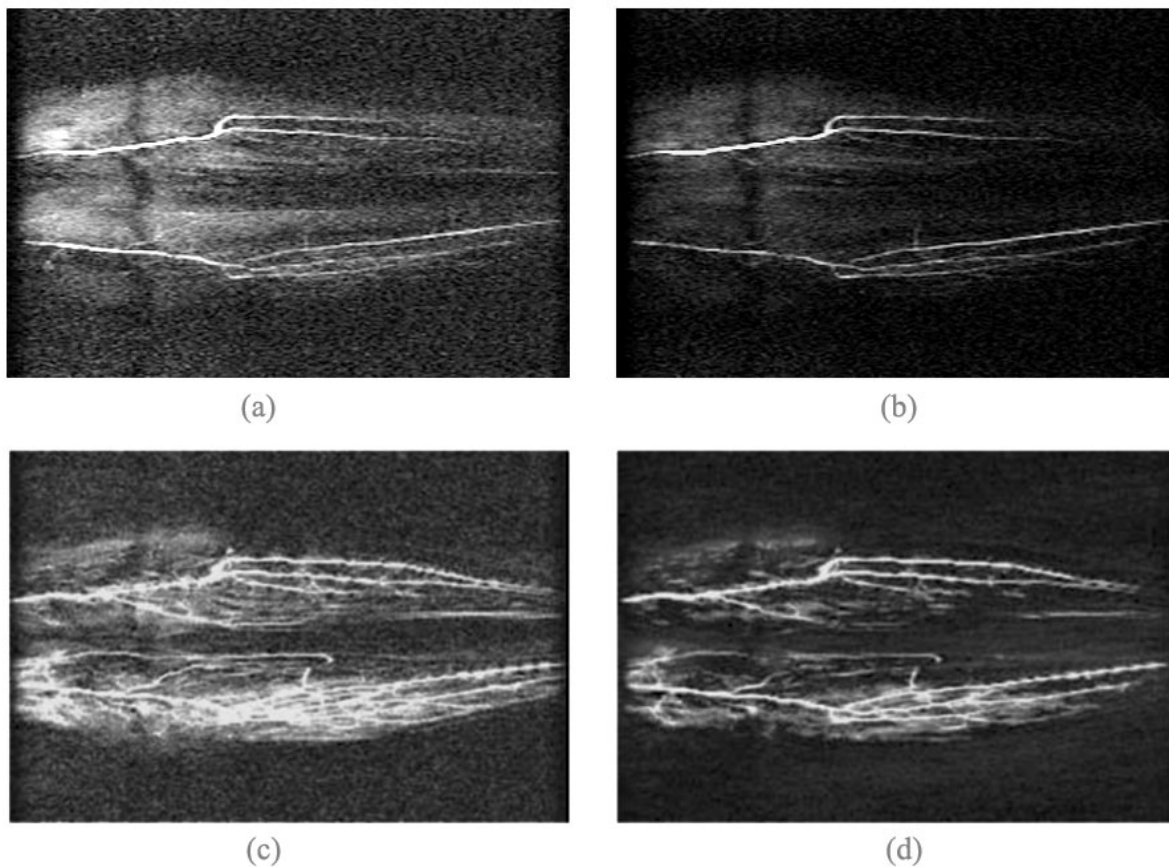


Figure 8: Motion Correction of clinical peripheral MRA case. (a) Motion corrupted difference image from two consecutive frames, and (b) Difference image after POCS correction. After this process was repeated for every corrupted frame, a summary angiogram was created automatically using the Automatic MRDSA program. (c) shows the manually obtained summary angiogram, and (d) shows the automatic summary angiogram after motion correction, demonstrating marked improvement in vascular delineation over (c).

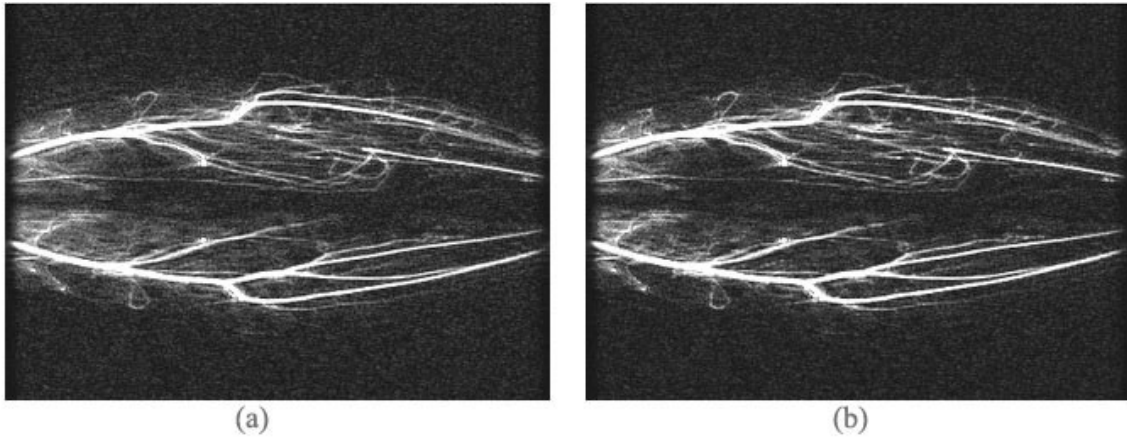


Figure 9: Clinical peripheral MRA example where little difference is seen between manual (a) and automatic (b) motion methods. There was little motion artifacts in this case.